

# Three-Dimensional Phosphorus-Doped Graphitic-C<sub>3</sub>N<sub>4</sub> Self-Assembly with NH<sub>2</sub>-Functionalized Carbon Composite Materials for Enhanced Oxygen Reduction Reaction

Yang Qiu,<sup>†</sup> Le Xin,<sup>‡</sup> Fan Jia,<sup>†</sup> Jian Xie,<sup>‡</sup> and Wenzhen Li<sup>\*,†,§</sup>

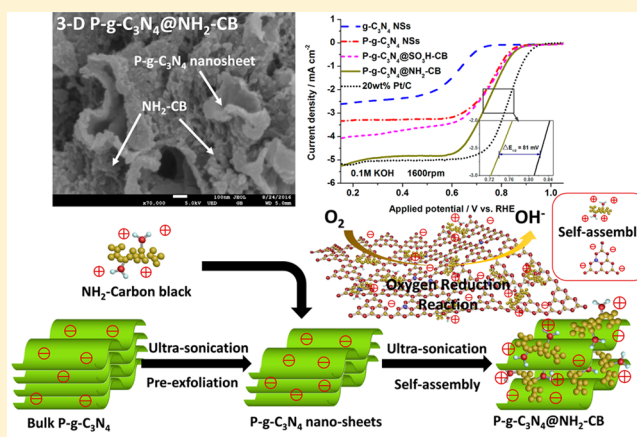
<sup>†</sup>Chemical and Biological Engineering, Biorenewables Research Laboratory, Iowa State University, Ames, Iowa50011, United States

<sup>‡</sup>Department of Mechanical Engineering, Purdue School of Engineering and Technology, Indiana University-Purdue University Indianapolis, Indianapolis, Indiana46202, United States

<sup>§</sup>US DOE Ames Lab, Ames, Iowa50011, United States

## Supporting Information

**ABSTRACT:** Oxygen reduction reaction (ORR) is the major reaction that occurs at the cathodes of fuel cells and metal–air batteries. Development of inexpensive, active, and durable heteroatom doped carbon-based ORR catalysts can lead to significant cost reduction of these electrochemical energy devices, which therefore has recently attracted enormous research attentions. This work reports a three-dimensional porous composite (P-g-C<sub>3</sub>N<sub>4</sub>@NH<sub>2</sub>-CB) for the highly efficient ORR catalyst. P-g-C<sub>3</sub>N<sub>4</sub>@NH<sub>2</sub>-CB was prepared by mixing phosphorus-doped graphitic carbon nitride nanosheets (P-g-C<sub>3</sub>N<sub>4</sub> NSs) with NH<sub>2</sub>-functionalized carbon black (NH<sub>2</sub>-CB) via a novel self-assembly approach. The NH<sub>2</sub>-CB was rationally chosen as the spacer that enables the self-assembled with the P-g-C<sub>3</sub>N<sub>4</sub> NSs driven by the electrostatic interaction. The intercalation of NH<sub>2</sub>-CB induces the transformation of 2-D P-g-C<sub>3</sub>N<sub>4</sub> NSs into a 3-D composites material of higher surface area, thereby exposing more ORR active sites. The P-g-C<sub>3</sub>N<sub>4</sub>@NH<sub>2</sub>-CB exhibited a remarkable ORR activity with an electron transfer number of 3.83 and Tafel slope of 89 mV dec<sup>-1</sup> in alkaline electrolyte, which is comparable to the ORR performance on Pt/Vulcan XC-72. It is found that the incorporated P atoms as well as employing NH<sub>2</sub>-CB spacer not only reduces the overpotential of ORR, but also enhances the ORR activity of carbon nitride-based materials, owing to the synergistic effect between P and N in tri-s-triazine rings of carbon nitrides and the optimum interaction between the oppositely charged P-g-C<sub>3</sub>N<sub>4</sub> and NH<sub>2</sub>-CB.



## 1. INTRODUCTION

The sustainable energy conversion and storage technologies, such as fuel cells and metal–air batteries, have attracted enormous attention and have been extensively studied and developed to meet the fast-growing global energy demands.<sup>1,2</sup> Oxygen reduction reaction (ORR), is the major cathodic reaction that drives the operations of the rechargeable metal–air batteries and fuel cells.<sup>3–8</sup> The noble metal-based catalysts, such as Pt, Pd, etc., have been considered as the most efficient catalysts for ORR at low temperatures. However, their high cost, scarcity, and poor durability significantly hinders their widespread applications.<sup>9–12</sup> With the aim of mitigating these barriers, considerable studies are focusing on lowering the noble metal content, which include the alloying with 3d group transition metals (e.g., PdFe) and/or the development of cheap metal oxides (e.g., Mn<sub>3</sub>O<sub>4</sub>, CoO/Co).<sup>13–15</sup> Recently, the N-doped carbon nanotube (CNT) was reported with a remarkable ORR activity,<sup>16</sup> and S-doping of graphene and

CNT also exhibited desirable electrocatalytic activity for ORR in alkaline media.<sup>17</sup> The heteroatoms (e.g., N, S) in carbon frameworks are found to enable tuning the charge density and spin density of neighboring C atoms, thereby promoting the adsorption of oxygen and facilitating the subsequent reduction reactions on carbon materials.<sup>18,19</sup> In this regard, numerous metal-free carbon materials doped with earth-abundant elements, such as B, N, S, and Cl, etc., have been extensively studied featuring the remarkable ORR activity and robust electrochemical stability.<sup>17,18,20–24</sup> However, P-doped materials are rarely reported and the improved ORR activity during P-doping requires further investigation.

Graphitic carbon nitrides (g-C<sub>3</sub>N<sub>4</sub>) have recently emerged as one of the novel electrocatalytic and photocatalytic materials

Received: July 6, 2016

Revised: October 29, 2016

Published: November 2, 2016

for ORR, oxygen evolution reaction (OER), and hydrogen evolution reaction (HER) owing to their high content of N, low cost, and unique tri-s-triazine ring structure.<sup>25–31</sup> The N atom involved can significantly enhance the stability of the heptazine rings due to the large conjugated  $\pi$  bonding in the carbon frameworks, which is believed to promote their catalytic activity toward specific electrochemical reactions.<sup>25</sup> On the other hand, the synthesis of g-C<sub>3</sub>N<sub>4</sub> via thermal polycondensation of nonmetal precursors resolves the concerns regarding to the contribution of trace metal impurities to the recorded ORR activity. However, the bulk g-C<sub>3</sub>N<sub>4</sub> with the small surface area (<20 m<sup>2</sup> g<sup>-1</sup>) and low electronic conductivity severely compromises its electrocatalytic activity.<sup>25,29</sup> To obtain the two-dimensional (2-D) thin layered g-C<sub>3</sub>N<sub>4</sub> nanosheets (g-C<sub>3</sub>N<sub>4</sub> NSs) with desirable electrochemical properties, three general approaches were applied, including (1) liquid exfoliation;<sup>26,28</sup> (2) thermal oxidation etching;<sup>25</sup> (3) acid–base-treatment.<sup>30</sup> These methods successfully increased the interlayer distance of bulk-C<sub>3</sub>N<sub>4</sub>, leading to a larger surface area with more exposed active sites, thus promoting its activity for ORR. However, the issues associated with the low yield, long sonication treatment (>10 h) and more importantly, the restacking of g-C<sub>3</sub>N<sub>4</sub> nanosheets upon drying makes them less promise to substitute their counterpart of the noble metal catalysts. To this regard, the spacer was introduced to enlarge the interlayer space of g-C<sub>3</sub>N<sub>4</sub> nanosheets.<sup>31,32</sup> However, the randomly mixing of g-C<sub>3</sub>N<sub>4</sub> spacers particles suffers from the inhomogeneity and their poor electronic interaction, which could then sacrifice the access of O<sub>2</sub> to some reactive sites on g-C<sub>3</sub>N<sub>4</sub>.

Herein, we demonstrate the three-dimensional (3-D) composite materials comprised of P-doped g-C<sub>3</sub>N<sub>4</sub> NSs and NH<sub>2</sub>-functionalized carbon black (CB) as an efficient ORR catalyst (P-g-C<sub>3</sub>N<sub>4</sub>@NH<sub>2</sub>-CB). The NH<sub>2</sub>-CB with positively charged surface was rationally introduced to insert into the negative charged P-g-C<sub>3</sub>N<sub>4</sub> nanosheet. Their strong electrostatic interaction induced by the surface functionalization of the spacer particles facilitates the distance enlargement and exfoliation of P-g-C<sub>3</sub>N<sub>4</sub> layered structure. As a result, NH<sub>2</sub>-CB particles were found to uniformly distribute on both sides of P-g-C<sub>3</sub>N<sub>4</sub> with a reduced thickness. The obtained P-g-C<sub>3</sub>N<sub>4</sub>@NH<sub>2</sub>-CB is believed to expose more sites (surface area of 286 m<sup>2</sup> g<sup>-1</sup>) for ORR and exhibits desirable electrical and chemical properties. In addition, the incorporation of P heteroatoms into tri-s-triazine rings of g-C<sub>3</sub>N<sub>4</sub> further boosts the ORR performance (electron transfer number of 3.83, at 0.4 V vsRHE), which is much higher than that of pristine g-C<sub>3</sub>N<sub>4</sub> material and even comparable to Pt/C in alkaline media. The impressive ORR activity, good electrical properties, as well as robust stability of P-g-C<sub>3</sub>N<sub>4</sub>@NH<sub>2</sub>-CB show great potential for application in the next generation of energy storage and conversion devices.

## 2. EXPERIMENTAL SECTION

**2.1. Material Preparation.** **2.1.1. Synthesis of Phosphorus-Doped Carbon Nitride Nanosheets (P-g-C<sub>3</sub>N<sub>4</sub> NSs).** The P-g-C<sub>3</sub>N<sub>4</sub> NSs were synthesized by mixing 0.1 g nitrilotris(methylene)-triphosphonic acid with 1.0 g dicyandiamide followed by thermal polycondensation process under 600 °C static air for 4h at a heating rate of 10 °C min<sup>-1</sup>. The green product (bulk P-g-C<sub>3</sub>N<sub>4</sub>) was collected after cooling down. Subsequently, 100 mg of the obtained bulk P-g-C<sub>3</sub>N<sub>4</sub> was well dispersed in the iso-propanol subjected ultrasonication for 5 h to form 0.5 mg mL<sup>-1</sup> suspension. The mixture was then centrifuged at 3000 rpm for 20 min to separate the nonexfoliated

aggregates, while the supernatant was further centrifuged at 8000 rpm for 10 min, washed thoroughly with deionized water, and freeze-dried to produce P-g-C<sub>3</sub>N<sub>4</sub> NSs.

**2.1.2. Synthesis of 3-D Composite of Phosphorus-Doped Carbon Nitride Nanosheets with NH<sub>2</sub>- or SO<sub>3</sub>H-Functionalized Carbon Black (P-g-C<sub>3</sub>N<sub>4</sub>@NH<sub>2</sub>-CB or P-g-C<sub>3</sub>N<sub>4</sub>@SO<sub>3</sub>H-CB).** The NH<sub>2</sub>-CB aqueous solution was drop-wisely added into the above P-g-C<sub>3</sub>N<sub>4</sub> NSs supernatant alcohol mixture with the uniform dispersity. The dispersion containing P-g-C<sub>3</sub>N<sub>4</sub> NSs and NH<sub>2</sub>-CB with the weight ratio of 3:1 of NH<sub>2</sub>-CB was then transferred into a Teflon-lined reactor (50 mL) for hydrothermal aging at 100 °C for 5 h. The self-assembly of NH<sub>2</sub>-CB and P-g-C<sub>3</sub>N<sub>4</sub> NSs was then initiated, which was driven by their acid–base interaction. After cooled down to room temperature, the P-g-C<sub>3</sub>N<sub>4</sub>@NH<sub>2</sub>-CB or P-g-C<sub>3</sub>N<sub>4</sub>@SO<sub>3</sub>H-CB was separated by the centrifuged at 10000 rpm for 5 min and freeze-dried. The P-g-C<sub>3</sub>N<sub>4</sub>@SO<sub>3</sub>H-CB was synthesized by using above method except the NH<sub>2</sub>-CB replacement by SO<sub>3</sub>H-CB (see NH<sub>2</sub>-CB and SO<sub>3</sub>H-CB synthesis details in the Supporting Information).<sup>33,34</sup>

**2.2. Material Characterization.** The samples were characterized by Rigaku Ultima IV X-ray diffraction (XRD) with Cu K $\alpha$  radiation ( $\lambda$  = 1.5406 Å) at a tube current of 44 mA and a tube voltage of 40 kV. The Brunauer–Emmett–Teller (BET) specific surface area and pore volume of the samples were characterized by using N<sub>2</sub> sorption/desorption measurement, which was carried out on a Quantachrome Autosorb iQ gas sorption analyzer, and the pore size distribution was calculated based on the NL-DFT model assuming a slit-shape pore structure.

JEOL 2100 200 kV scanning and transmission electron microscope (STEM) and FEI Quanta 250 field-emission scanning electron microscope (SEM) coupled with the element energy-dispersive X-ray spectrometer (EDS) were employed to characterize the catalyst morphology and the element distribution. Atomic force microscopy (AFM) images were obtained using a Dimension 3100 scanning probe microscope with Nanoscope IV controller (Veeco Metrology LLC.). All AFM measurements were conducted in tapping mode with a mica employed as substrate. Fourier transform infrared reflection (FTIR) spectra were obtained with the IR spectrometer, Thermo Scientific Nicolet iS 50. X-ray photoelectron spectroscopy (XPS) with Mg K alpha X-ray (1253.6 eV) (Kratos Amicus/ESCA 3400) was used to determine the heteroatom concentrations and its corresponding chemical/valence status through different binding energy peaks. Zeta potential results were obtained by Malvern NanoZS Zetasizer with Auto-Titrator.

**2.3. Electrocatalytic Characterization.** The electrochemical tests were carried out in the three-electrode half-cell, which consists of a glassy carbon rotating disk electrode (RDE, 0.19625 cm<sup>2</sup> geometric surface area) (working electrode, Pine), a coiled platinum counter electrode, and a Hg/HgO reference electrode with 0.1 M KOH filling solution. The applied potential was controlled using a multichannel potentiostat (VMP-300 Biological). To fabricate the working electrode, a 2.0 mg mL<sup>-1</sup> catalyst ink was prepared by dispersing P-g-C<sub>3</sub>N<sub>4</sub>@NH<sub>2</sub>-CB in mixture of the iso-propanol and 5 wt % Nafion solution (iso-propanol: Nafion solution =9:1 v/v), followed by ultrasonication until no aggregation was visible. Then, 30  $\mu$ L ink was dropped onto the surface of a RDE with a catalyst loading of 0.306 mg cm<sub>geo</sub><sup>-2</sup>. A uniform catalyst film was obtained after 30 min ambient temperature drying in air. The control samples, including g-C<sub>3</sub>N<sub>4</sub> NSs, P-g-C<sub>3</sub>N<sub>4</sub> NSs, and 20 wt % Pt/C, were fabricated using the same method described above, and the loading of Pt was 61.2  $\mu$ g<sub>Pt</sub> cm<sub>geo</sub><sup>-2</sup>. The ORR performance of the catalyst was investigated by cyclic voltammetry (CV) performed at 50 mV s<sup>-1</sup> scan rate with N<sub>2</sub> or O<sub>2</sub> purging, respectively. The linear sweep voltammetry (LSV) tests were conducted at different rotating rate from 2000 to 400 rpm in O<sub>2</sub>-saturated 0.1 M KOH with 10 mV s<sup>-1</sup> scan rate.

The overall number of electrons transferred per oxygen molecule,  $n$ , in ORR were calculated according to the slopes of the Koutecky–Levich plots using the following equations:<sup>13,22</sup>

$$\frac{1}{J} = \frac{1}{J_L} + \frac{1}{J_k} = \frac{1}{B\omega^{1/2}} + \frac{1}{J_k}$$

Scheme 1. Schematic of the Preparation of Three-Dimensional Phosphorus-Doped Graphitic Carbon Nitride Self-Assembly with  $\text{NH}_2$ -Functionalized Carbon Composite Catalyst,  $\text{P-g-C}_3\text{N}_4@/\text{NH}_2\text{-CB}$

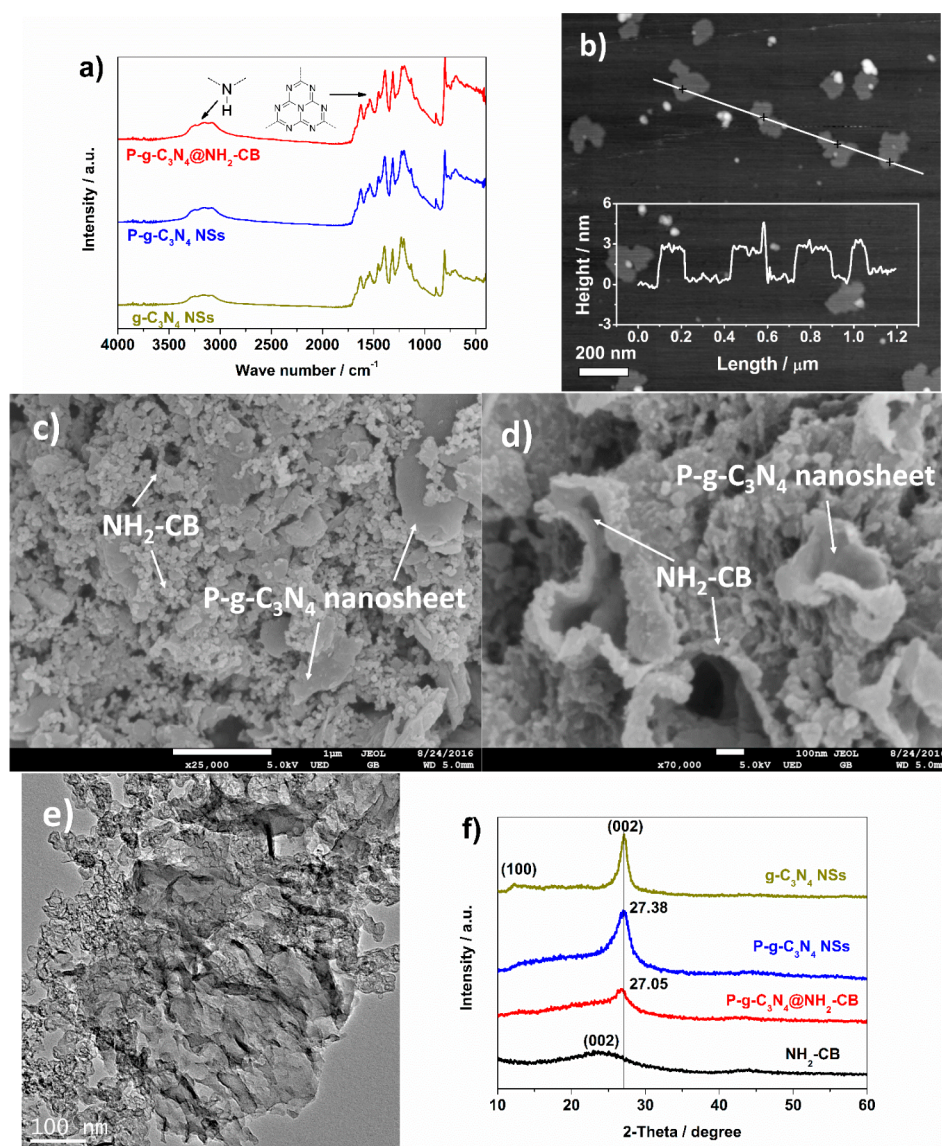
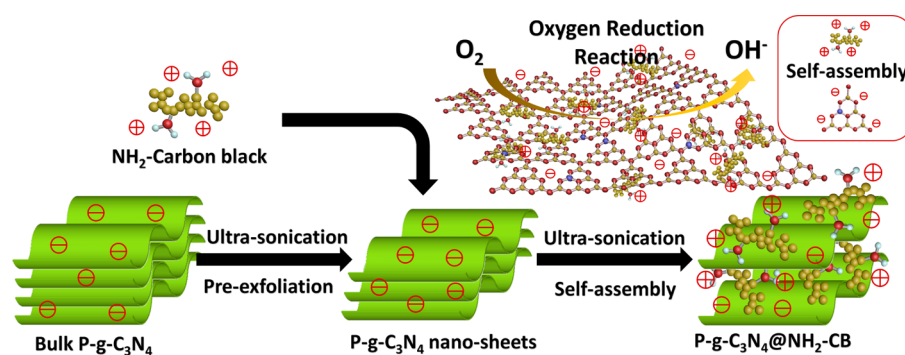


Figure 1. (a,f) FTIR and XRD patterns of  $\text{g-C}_3\text{N}_4$ - and  $\text{P-g-C}_3\text{N}_4$ -based materials; (b) AFM image of  $\text{P-g-C}_3\text{N}_4$  NSs; (c,d) SEM images and (e) TEM images of  $\text{P-g-C}_3\text{N}_4@/\text{NH}_2\text{-CB}$ .

$$B = 0.2nFC_0(D_0)^{2/3}\nu^{-1/6}$$

where  $J$  is the measured current density,  $J_k$  and  $J_L$  are the kinetic and diffusion limiting current densities,  $\omega$  is the electrode rotating speed in rpm,  $B$  is the reciprocal of the slope,  $n$  is the number of electrons transferred per oxygen molecule,  $F$  is the Faraday constant (96485 C

$\text{mol}^{-1}$ ),  $D_0$  is the diffusion coefficient of  $\text{O}_2$  in 0.1 M KOH ( $1.9 \times 10^{-5} \text{ cm}^2 \text{ s}^{-1}$ ),  $\nu$  is the kinetic viscosity ( $0.01 \text{ cm}^2 \text{ s}^{-1}$ ), and  $C_0$  is the concentration of  $\text{O}_2$  ( $1.2 \times 10^{-3} \text{ mol L}^{-1}$ ).<sup>22,28</sup> The constant 0.2 is adopted when the rotating speed is in rpm.

Rotating ring-disk electrode (RRDE) was employed to measure the concentration of  $\text{HO}_2^-$  intermediate and electron transfer number per oxygen ( $n$ ) with scanning rate of  $10 \text{ mV s}^{-1}$  at rotating rate of 1600 rpm. The  $\text{HO}_2^-$  intermediated, generated on the surface of disk electrode ( $0.19625 \text{ cm}^2$  geometric surface area), can be immediately oxidized on Pt-ring electrode with a potential applied at 0.8 V vs RHE. The electron transfer number  $n$  and the percentage of  $\text{HO}_2^-$  intermediate produced ( $\text{HO}_2^- \%$ ) can be determined as follows:<sup>22</sup>

$$n = 4 \times \frac{I_d}{I_d + I_r/N}$$

$$\text{HO}_2^- \% = 200 \times \frac{I_r/N}{I_d + I_r/N}$$

where  $I_d$  is the disk current;  $I_r$  is the ring current, and  $N$  is the ring current collection efficiency which was determined to be 23%.<sup>22,35</sup>

Electrochemical impedance spectroscopy (EIS) measurements were performed by applying an AC voltage at 0.4 V vs RHE with 5 mV amplitude in a frequency range from 100 kHz to 10 mHz in  $\text{O}_2$ -saturated 0.1 M KOH solution. The 20 cycles CV scanning were conducted prior to the EIS measurements to obtain stable CV polarization curves, and the EIS measurement will be subsequently performed without rotation.<sup>36</sup> All experimental results for the ORR activity in this paper were reported as current density versus applied potential (vs RHE), and the current densities were normalized using geometric surface area of a glassy carbon electrode with 5 mm diameter. The Hg/HgO reference electrode was calibrated with respect to the reversible hydrogen electrode (RHE) before use. The calibration was conducted in standard three-electrode system with Pt wire as the working and counter electrodes, and the Hg/HgO electrode as the reference electrode. Before the calibration, the 0.1 M KOH electrolyte was purged and saturated with high purity  $\text{H}_2$  for 30 min, and LSV was then carried out at a scan rate of  $0.5 \text{ mV s}^{-1}$  from  $-0.93 \text{ V}$  to  $-0.85 \text{ V}$  vs Hg/HgO. The potential (vs 0.1 M KOH Hg/HgO electrode) at which current crosses zero is recorded as 0.888 V versus the reversible hydrogen electrode ( $E_{(\text{RHE})} = E_{(\text{Hg}/\text{HgO})} + 0.888 \text{ V}$  in 0.1 M KOH electrolyte).

### 3. RESULTS AND DISCUSSION

**3.1. Material Synthesis and Characterization.** The bulk P-g- $\text{C}_3\text{N}_4$  materials were prepared via the thermal polycondensation approach as described in the [Experimental Section](#), which has been reported as the procedure for bulk g- $\text{C}_3\text{N}_4$  synthesis.<sup>26,29</sup> With the successful incorporation of P atom, the color of bulk g- $\text{C}_3\text{N}_4$  changes from yellow to green (bulk P-g- $\text{C}_3\text{N}_4$ ). Since the obtained carbon nitride layers tend to restack through  $\pi$ - $\pi$  interaction, it is believed that only limited active sites on bulk P-g- $\text{C}_3\text{N}_4$  surface could access  $\text{O}_2$ , significantly inhibiting its electrocatalytic activity for ORR. Therefore, the exfoliation process is required to prepare thinner layered carbon nitride based materials with the aim of exposing more active sites for catalyzing the electrochemical reaction. In addition, the electronic properties of the carbon nitride materials could be also enhanced through effective exfoliation.<sup>25,26</sup> As illustrated in [Scheme 1](#), the as-synthesized bulk P-g- $\text{C}_3\text{N}_4$  of the multilayered structure were pre-exfoliated through ultrasonication conducted in a solvent to make P-g- $\text{C}_3\text{N}_4$  NSs. In order to achieve the optimum exfoliation performance, the solvent effects on the efficiency of the carbon nitride exfoliation were studied. Bulk g- $\text{C}_3\text{N}_4$  was dispersed in different solvents with the same concentration, including isopropanol (IPA), *N*-methyl-pyrrolidone (NMP), water, ethanol, acetone, and hexane, followed by ultrasonication for 2 h. As a result ([Figure S1](#)), the bulk g- $\text{C}_3\text{N}_4$  was homogeneously dispersed in IPA and NMP without apparent aggregation, indicating an effective exfoliation, while large precipitations can

be clearly observed in other solvents after the extended sonication. It is noteworthy that the exfoliation performance could be significantly influenced by the surface energies of the solvents used, and the layered structure can be successfully exfoliated when the enthalpy of mixing is minimized, as the surface energies of flake were close to that of the solvent used.<sup>24</sup> Therefore, IPA and NMP (ca.  $40 \text{ mJ m}^{-2}$  surface energy)<sup>24</sup> are more favorable for exfoliating the carbon nitride sheets (ca.  $70 \text{ mJ m}^{-2}$  surface energy),<sup>25</sup> which agrees well with the experimental results. However, the high boiling point of NMP could lead to the aggregation of the exfoliated g- $\text{C}_3\text{N}_4$  NSs owing to the slow solvent evaporation. Thus, IPA of low boiling point was chosen to exfoliate the P-g- $\text{C}_3\text{N}_4$  based materials in this work. After 5 h ultrasonication pre-exfoliation, most of bulk P-g- $\text{C}_3\text{N}_4$  particles were dispersed in IPA to form a uniformly stable solution. The P-g- $\text{C}_3\text{N}_4$  NSs were finally obtained by collecting the precipitants via the centrifuge separation at 3000 rpm.

The collected P-g- $\text{C}_3\text{N}_4$  NSs were characterized by infrared spectroscopy (IR) and atomic force microscopy (AFM). As shown in [Figure 1a](#), the P-g- $\text{C}_3\text{N}_4$  NSs exhibits very similar IR spectrum as g- $\text{C}_3\text{N}_4$  NSs, and all characteristic peaks of tri-s-triazine structure of g- $\text{C}_3\text{N}_4$  were well preserved in P-g- $\text{C}_3\text{N}_4$  NSs IR spectrum, indicating the 2-D layered structure has no significant change after the phosphorus doping. The broad peaks between  $3400$  and  $3000 \text{ cm}^{-1}$  of P-g- $\text{C}_3\text{N}_4$  can be assigned to the N-H stretches in amino groups ( $-\text{NH}_2$  or  $=\text{NH}$ ),<sup>25</sup> suggesting the partial hydrogenation of some nitrogen atoms in the nanosheets. The sharp peak at around  $809 \text{ cm}^{-1}$  is originated from the heptazine ring structure, and those peaks in the region from  $1800$  to  $900 \text{ cm}^{-1}$  are attributed to the typical stretching modes of aromatic C-N heterocycles.<sup>26,37</sup> It should be noted that the peaks corresponding to P-N groups likely overlap with that of C-N heterocycles, making it difficult to be differentiated owing to the low P content.<sup>38</sup> AFM was then employed to determine the thickness of pre-exfoliated P-g- $\text{C}_3\text{N}_4$  NSs. The resulting thickness was measured to be approximate 3 nm ([Figure 1b](#)), suggesting the 2-D structure consisted of approximately 8–10 C-N atomic layers.<sup>28</sup> However, these pre-exfoliated P-g- $\text{C}_3\text{N}_4$  NSs were found to seriously restack upon drying. Thus, the  $\text{NH}_2$ -functionalized carbon black particles were introduced as a spacer to stabilize the pre-exfoliated P-g- $\text{C}_3\text{N}_4$  NSs, by which the insertion of  $\text{NH}_2$ -CB into P-g- $\text{C}_3\text{N}_4$  NSs induces the transformation to a 3-D porous interconnected network.

As illustrated in [Scheme 1](#), the positively charged  $\text{NH}_2$ -CB particles (zeta potential of  $-27.3 \text{ eV}$ , [Figure S2](#)) were added into the IPA solution suspended with pre-exfoliated P-g- $\text{C}_3\text{N}_4$  NSs (zeta potential of  $+72.0 \text{ mV}$  [Figure S2](#)) of the weight ratio of 1:3 ( $\text{NH}_2$ -CB: P-g- $\text{C}_3\text{N}_4$  NSs). Their strong electrostatic interaction induced by the surface functionalization of the spacer particles facilitates the exfoliation of P-g- $\text{C}_3\text{N}_4$  layered structure. As a result,  $\text{NH}_2$ -CB particles were found to uniformly distribute on both sides of P-g- $\text{C}_3\text{N}_4$  NSs, leading to a reduced thickness ([Figure 1c,d](#)). Unlike the 2-D stacked P-g- $\text{C}_3\text{N}_4$  NSs ([Figure S3a](#)), the 3-D porous P-g- $\text{C}_3\text{N}_4$ @ $\text{NH}_2$ -CB composite was formed with  $\text{NH}_2$ -CB as the pillar to mitigate the issue of P-g- $\text{C}_3\text{N}_4$  NSs restacking, as confirmed by the SEM images ([Figure 1c,d](#)). When it changed the weight ratio of two components from 1:3 ( $\text{NH}_2$ -CB: P-g- $\text{C}_3\text{N}_4$  NSs) to 3:1, a homogeneous  $\text{NH}_2$ -CB outer layer of higher density was observed to cover the surface of P-g- $\text{C}_3\text{N}_4$  NSs, indicating a good assembling of  $\text{NH}_2$ -CB and P-g- $\text{C}_3\text{N}_4$  NSs via the

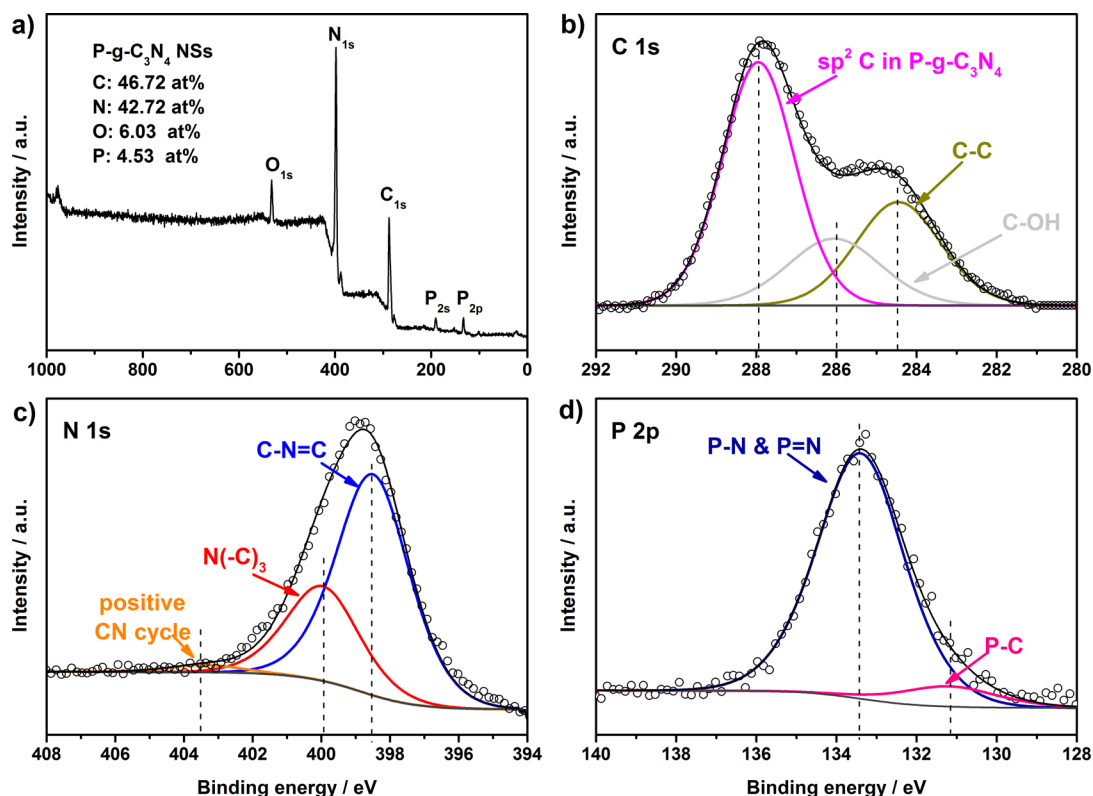


**Figure 2.** (a) XPS survey spectrum and high-resolution spectra of (b)  $C_{1s}$ , (c)  $N_{1s}$ , and (d)  $P_{2p}$  of P-g- $C_3N_4$  NSs.

electrostatic interaction (Figure S3b). With the  $NH_2$ -CB spacer intercalation, the BET surface area of P-g- $C_3N_4$ @ $NH_2$ -CB was significantly increased to  $286\text{ m}^2\text{ g}^{-1}$  ( $10\text{ m}^2\text{ g}^{-1}$  for bulk P-g- $C_3N_4$ ) (Figure S4), which is consistent with the highly porous structure shown in SEM images. The as-synthesized 3-D porous P-g- $C_3N_4$ @ $NH_2$ -CB composite was also characterized by TEM. The  $NH_2$ -CB particles were sandwiched in between P-g- $C_3N_4$  NSs (Figure 1d, S3c), and the nearly transparent layers demonstrate the very thin layers, this is in good consistence with the results obtained from SEM images and further confirms a good assembly driven by the acid–base interaction. It is noteworthy that the tri-s-triazine structure was well maintained in P-g- $C_3N_4$ @ $NH_2$ -CB, and all peaks featuring heptazine heterocycles, e.g. peaks of  $3400\text{--}3000\text{ cm}^{-1}$ ,  $809\text{ cm}^{-1}$ , and  $1800\text{--}900\text{ cm}^{-1}$ , were clearly observed in the IR spectrum (Figure 1a).

Additionally, X-ray diffraction (XRD) was used to analyze the CN structure of P-g- $C_3N_4$  based materials. As shown in Figure 1f, the clear diffraction peak at  $27.38^\circ$ , assigned to (002) interlayer diffraction of a CN graphitic-like structure,<sup>26,28</sup> was observed on both g- $C_3N_4$  NSs and P-g- $C_3N_4$  NSs, indicating a well maintaining of the tri-s-triazine ring structure in P-g- $C_3N_4$  NSs upon P doping. On the other hand, the low-angle diffraction peak at  $2\theta$  of  $13.3^\circ$  (in-planar repeated tri-s-triazine units) becomes less obvious when the g- $C_3N_4$  NSs is exfoliated from bulk g- $C_3N_4$  (Figure S5), and the intensity is further reduced with P atoms incorporation. This could be mainly caused by reduced amount of stacked carbon nitride interlayers after pre-exfoliation and smaller planar size of the repeated tri-s-triazine unit disordered by P atoms.<sup>25,28</sup> Furthermore, it is interesting to note that a typical (002) diffraction represented by CN graphitic-like structure slightly shifts from  $27.38^\circ$  to  $27.05^\circ$  when the  $NH_2$ -CB spacer inserts into pre-exfoliated P-

g- $C_3N_4$  NSs, highlighting the 3-D porous composite formation with an enlarged space between P-g- $C_3N_4$  interlayers.<sup>25</sup>

To investigate the composition and N and P valence states of the as-synthesized P-g- $C_3N_4$ , the pre-exfoliated P-g- $C_3N_4$  NSs were characterized by X-ray photoelectron spectroscopy (XPS). Since the inserted  $NH_2$ -CB spacer could affect the XPS signals of P-g- $C_3N_4$  NSs, XPS was conducted by using pre-exfoliated P-g- $C_3N_4$  NSs in the absence of  $NH_2$ -CB particles. From Figure 2a, the atomic ratio of P-g- $C_3N_4$  NSs were determined to be 46.72% of C, 42.72% of N, 6.03% of O, and 4.53% of P. The C/N ratio of P-g- $C_3N_4$  NSs was calculated to be 1.09, which is higher than that of 0.83 in g- $C_3N_4$  (Figure S6), indicating a successful incorporation of both P and C during the thermal polycondensation. The spectra of  $P_{2p}$ ,  $C_{1s}$  and  $N_{1s}$  were further characterized as shown in Figure 2b–d. A broad peak was observed in the  $P_{2p}$  narrow scan spectrum (Figure 2d), which can be deconvoluted into two peaks, located at 131.2 eV, and 133.5 eV, respectively. Since the binding energy of the P–C coordination should be 1–2 eV lower than that of P–N/P=N species, the 131.2 eV peak is originated from the P–C structure, while another peak at 133.5 eV can be assigned to P–N and P=N structures.<sup>38–40</sup> The high resolution of  $C_{1s}$  spectrum of P-g- $C_3N_4$  NSs (Figure 2b) can be deconvoluted into three major peaks centered at 288.0, 286.0, and 284.6 eV, respectively. The peak located at 288.0 eV is well identified as a  $sp^2$ -hybridized carbon in an N-containing aromatic ring (N–C=N), which is the main structure of g- $C_3N_4$  as shown in Figure S6a, and the 284.6 eV peak could be assigned to  $sp^2$  C–C bonds.<sup>26,28</sup> In addition, more O atoms were added due to the P doping, and the peak located at 286.0 eV was originated from C–OH structure, whose relative ratio is much larger than that of g- $C_3N_4$  with low O atom concentration. Meanwhile, the  $N_{1s}$  spectrum (Figure 2c) can be deconvoluted into three different

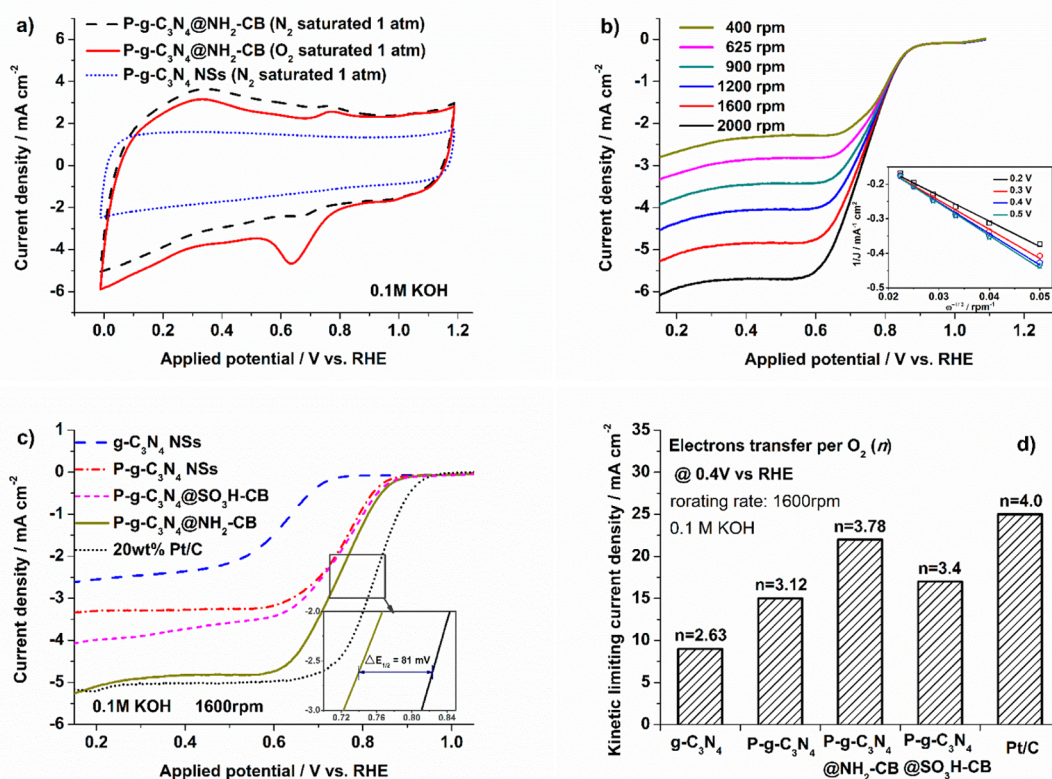


**Figure 3.** (a) Cyclic voltammograms (CV) of P-g-C<sub>3</sub>N<sub>4</sub>@NH<sub>2</sub>-CB in 0.1 M KOH solution saturated with N<sub>2</sub> (dash line) and O<sub>2</sub> (solid line) at a scan rate of 50 mV s<sup>-1</sup>. (b) ORR Polarization curves at different rotating speeds for P-g-C<sub>3</sub>N<sub>4</sub>@NH<sub>2</sub>-CB in O<sub>2</sub>-saturated 0.1 M KOH solution at a scan rate of 10 mV s<sup>-1</sup> (the inset shows the corresponding K-L plots). (c) Comparative polarization curves of different catalysts with the same loading measured at 1600 rpm in O<sub>2</sub>-saturated 0.1 M KOH electrolyte. (d) Kinetic limiting current density ( $J_k$ ) and the electron transfer number for g-C<sub>3</sub>N<sub>4</sub> NSs, 20 wt % Pt/C, and P-g-C<sub>3</sub>N<sub>4</sub> based catalysts at 0.4 V.

peaks with the binding energy of 398.6, 399.9, and 403.5 eV, respectively. The major peak at 398.6 eV represents a typical structure of sp<sup>2</sup>-hybridized nitrogen in C-containing triazine rings (C–N=C), while the peak at 399.9 eV is assigned to the tertiary nitrogen N(C)<sub>3</sub> structure.<sup>28,41</sup> The absence of the peak around 401.0 eV suggests that the samples do not contain the N–N bonding structure.<sup>25</sup> In comparison, the small peak located at 403.5 eV was also detected, which could be attributed to charging effect or the localization of positive charges in heterocycles and the cyano- group.<sup>28</sup> Based on the obtained XPS results, the P atoms were successfully incorporated into C–N frameworks of P-g-C<sub>3</sub>N<sub>4</sub> NSs, while its 2-D heptazine layered structure was well preserved.

The self-assembly between P-g-C<sub>3</sub>N<sub>4</sub> NSs and NH<sub>2</sub>-CB spacer proven by SEM and TEM results is driven by a strong electrostatic interaction, ascribing to the opposite surface charge (zeta potential of –27.3 eV for P-g-C<sub>3</sub>N<sub>4</sub> NSs; +72.0 eV for NH<sub>2</sub>-CB). Since the surface charge of P-g-C<sub>3</sub>N<sub>4</sub> and spacer could significantly affect the self-assembling performance, thereby determining the resulting composite structure, the carbon particles with different functionalities were studied. The positively charged NH<sub>2</sub>-CB spacer (zeta potential of +72.0 eV, Figure S2) was rationally replaced by negatively charged SO<sub>3</sub>H-CB particles (zeta potential of –44.1 eV, Figure S2). In sharp contrast to the 3-D porous structure of P-g-C<sub>3</sub>N<sub>4</sub>@NH<sub>2</sub>-CB, the SO<sub>3</sub>H-CB particles were predominantly aggregated and populated on the P-g-C<sub>3</sub>N<sub>4</sub> surface instead of inserting into P-g-C<sub>3</sub>N<sub>4</sub> interlayers (Figure S3d,e). This could be attributed to the same type of surface charges between the P-g-C<sub>3</sub>N<sub>4</sub> NSs and SO<sub>3</sub>H-CB, causing a poor

interaction of SO<sub>3</sub>H-CB particles. Therefore, the 3-D porous structure of P-g-C<sub>3</sub>N<sub>4</sub>@NH<sub>2</sub>-CB should be attributed to the strong electrostatic interaction between P-g-C<sub>3</sub>N<sub>4</sub> and NH<sub>2</sub>-CB, which has a great potential as efficient metal-free electrocatalysts for ORR.

**3.2. Electrochemical Characterization.** Before the evaluation of electrocatalytic ORR activity, the Hg/HgO reference electrode was calibrated with respect to the reversible hydrogen electrode (RHE), which determines  $E_{(RHE)} = E_{(Hg/HgO)} + 0.888$  V in 0.1 M KOH electrolyte, as shown in Figure S7. All applied potentials in this paper were reported versus the reversible hydrogen electrode (RHE).

The electrocatalytic ORR activity of P-g-C<sub>3</sub>N<sub>4</sub>-based catalysts were first investigated by cyclic voltammetry (CV) tests. As shown in Figure 3a, P-g-C<sub>3</sub>N<sub>4</sub>@NH<sub>2</sub>-CB composite exhibits larger double-layer current density than that of 2-D P-g-C<sub>3</sub>N<sub>4</sub> NSs in N<sub>2</sub>-saturated 0.1 M KOH electrolyte (dash curve), attributing to the 3-D porous structure with larger surface area as the result of the insertion of NH<sub>2</sub>-CB particles. In contrast, P-g-C<sub>3</sub>N<sub>4</sub>@SO<sub>3</sub>H-CB composite reveals a smaller double-layer current density (lower surface area) as compared to that of P-g-C<sub>3</sub>N<sub>4</sub>@NH<sub>2</sub>-CB (Figure S8). When the electrolyte was saturated with O<sub>2</sub>, a well-defined cathodic ORR peak, centered at 0.63 V, was observed on P-g-C<sub>3</sub>N<sub>4</sub>@NH<sub>2</sub>-CB, indicating an ORR electrocatalytic activity.

To gain deeper insights into ORR on P-g-C<sub>3</sub>N<sub>4</sub> based catalysts, linear sweep voltammetry (LSV) tests were carried out at different rotating rates ranging from 2000 to 400 rpm in 0.1 M KOH O<sub>2</sub>-saturated electrolyte. The Koutecky–Levich equation (for K-L equation details see Experimental Section)

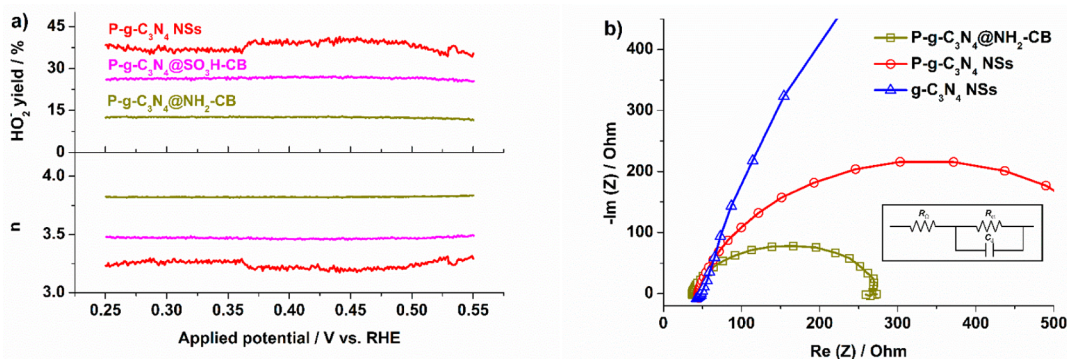


**Figure 4.** (a) HO<sub>2</sub><sup>-</sup> yields (top) during the ORR and the corresponding electron transfer number ( $n$ , bottom) on different catalysts measured by RRDE. (b) EIS Nyquist plots (recorded at 0.4 V) of P-g-C<sub>3</sub>N<sub>4</sub>@NH<sub>2</sub>-CB, P-g-C<sub>3</sub>N<sub>4</sub> NSs, and g-C<sub>3</sub>N<sub>4</sub> NSs (Inset: the equivalent circuit diagram).

was used to calculate the electron transfer number ( $n$ ) per O<sub>2</sub> at a given applied potential in the mass transport limiting current region. As shown in the inset of Figure 3b, the K-L plots ( $J^{-1}$  vs  $\omega^{-1/2}$ ) of the P-g-C<sub>3</sub>N<sub>4</sub>@NH<sub>2</sub>-CB catalyst exhibited a linear relationship within the applied potential ranging from 0.2 to 0.5 V, and the slopes of investigated plots were kept approximately constant, suggesting a similar  $n$  value and a stable ORR activity at the given potential range. The electron transfer number,  $n$ , was determined to be 3.78 at 0.4 V under 1600 rpm, indicating that the OH<sup>-</sup> (4e<sup>-</sup> transfer reaction) is the dominant product with a small amount of HO<sub>2</sub><sup>-</sup> produced following 2e<sup>-</sup> transfer pathway.

Comparative studies of the electrocatalytic activity of P-g-C<sub>3</sub>N<sub>4</sub>@SO<sub>3</sub>H-CB, P-g-C<sub>3</sub>N<sub>4</sub> NSs, and g-C<sub>3</sub>N<sub>4</sub> NSs with Pt/C were also conducted in O<sub>2</sub>-saturated alkaline electrolyte. When doped with P atom, the onset potential (potential at which  $J = 0.1 \text{ mA cm}^{-2}$ ) of P-g-C<sub>3</sub>N<sub>4</sub> NSs significantly shifts from 0.76 V (g-C<sub>3</sub>N<sub>4</sub>) to 0.87 V with 110 mV overpotential decrease. In addition, P-g-C<sub>3</sub>N<sub>4</sub> NSs exhibits a limiting current density of 3.40 mA cm<sup>-2</sup> at 0.4 V, which is much higher than 2.40 mA cm<sup>-2</sup> obtained from g-C<sub>3</sub>N<sub>4</sub> NSs (Figure 3c). The onset potential positive shift (overpotential decrease) as well as the limiting current density increase suggest the enhancement of ORR activity for P-g-C<sub>3</sub>N<sub>4</sub> NSs with the P atom incorporation. However, the ORR performance on P-g-C<sub>3</sub>N<sub>4</sub> NSs still requires further improvement as the restaking of P-g-C<sub>3</sub>N<sub>4</sub> NSs blocks a substantial amount of active sites and set a higher diffusion resistance of O<sub>2</sub> gas. In this regard, the composite of P-g-C<sub>3</sub>N<sub>4</sub>@NH<sub>2</sub>-CB or P-g-C<sub>3</sub>N<sub>4</sub>@SO<sub>3</sub>H-CB was prepared and demonstrated a further enhancement of the limiting current density of 4.87 mA cm<sup>-2</sup> at 0.4 V with a Tafel slope of 89 mV dec<sup>-1</sup> (Figure S9) for P-g-C<sub>3</sub>N<sub>4</sub>@NH<sub>2</sub>-CB, and 3.73 mA cm<sup>-2</sup> at 0.4 V with a Tafel slope of 92 mV dec<sup>-1</sup> (Figure S9) for P-g-C<sub>3</sub>N<sub>4</sub>@SO<sub>3</sub>H-CB, and the onset potential also positively shifts to 0.90 V (P-g-C<sub>3</sub>N<sub>4</sub>@NH<sub>2</sub>-CB) and 0.88 V (P-g-C<sub>3</sub>N<sub>4</sub>@SO<sub>3</sub>H-CB), respectively. However, owing to the same type of surface charge between SO<sub>3</sub>H-CB and P-g-C<sub>3</sub>N<sub>4</sub> NSs, it shows an inferior performance for 3-D P-g-C<sub>3</sub>N<sub>4</sub>@SO<sub>3</sub>H-CB composite that exhibits lower ORR activity than P-g-C<sub>3</sub>N<sub>4</sub>@NH<sub>2</sub>-CB, although it still outperforms 2-D structured P-g-C<sub>3</sub>N<sub>4</sub> NSs (limiting current density of 3.40 mA cm<sup>-2</sup> at 0.4 V with a Tafel slope of 98 mV dec<sup>-1</sup>). The strong electrostatic interaction between NH<sub>2</sub>-CB and P-g-C<sub>3</sub>N<sub>4</sub> NSs effectively drives to construct a 3-D porous P-g-C<sub>3</sub>N<sub>4</sub>@NH<sub>2</sub>-CB composite with larger surface area and more exposed ORR active sites. As a result, with the enhancement originated from incorporated P atoms and 3-D porous structure, the resulting 3-

D P-g-C<sub>3</sub>N<sub>4</sub>@NH<sub>2</sub>-CB composite exhibits the best ORR performance over all investigated carbon nitride-based materials reported in this work. To rule out effects of the functionalized carbon blacks on the improvement of the ORR performance observed on P-g-C<sub>3</sub>N<sub>4</sub>@NH<sub>2</sub>-CB and P-g-C<sub>3</sub>N<sub>4</sub>@SO<sub>3</sub>H-CB, the ORR activities of NH<sub>2</sub>-CB and SO<sub>3</sub>H-CB were also studied. As shown in Figure S10, the NH<sub>2</sub>-CB and SO<sub>3</sub>H-CB show the onset potential of 0.75 and 0.73 V with the limiting current of 3.5 mA cm<sup>-2</sup> and 2.8 mA cm<sup>-2</sup> at 0.4 V, respectively, revealing their poor ORR catalytic activities. Therefore, the NH<sub>2</sub>-CB spacer contributes a minor ORR activity on the remarkable ORR performance obtained with P-g-C<sub>3</sub>N<sub>4</sub>@NH<sub>2</sub>-CB, which should be predominantly originated from the 3-D porous structured P-g-C<sub>3</sub>N<sub>4</sub>.

The electron transfer number,  $n$ , of pristine g-C<sub>3</sub>N<sub>4</sub>, P-g-C<sub>3</sub>N<sub>4</sub> NSs, and P-g-C<sub>3</sub>N<sub>4</sub>@SO<sub>3</sub>H-CB calculated by using the K-L equation was 2.63, 3.12, and 3.40 at 0.4 V vs RHE, respectively, which was in good accordance to the trend of their respective limiting current density, but much lower than the  $n$  value of 3.78 for P-g-C<sub>3</sub>N<sub>4</sub>@NH<sub>2</sub>-CB. The kinetic limiting current density ( $J_k$ ) at 0.4 V determined by the K-L equation is shown in Figure 3d. The P-g-C<sub>3</sub>N<sub>4</sub>@NH<sub>2</sub>-CB shows the highest  $J_k$  of 22.1 mA cm<sup>-2</sup>, indicating an excellent ORR electrocatalytic activity that is very close to the  $J_k$  of 25.0 mA cm<sup>-2</sup> obtained from Pt/C. Although the half-wave potential difference ( $\Delta E_{1/2}$ ) of 81 mV was observed comparing the P-g-C<sub>3</sub>N<sub>4</sub>@NH<sub>2</sub>-CB and Pt/C, a comparable ORR performance at the mass transport limiting region with electron transfer number of 3.78 per O<sub>2</sub> holds promise for P-g-C<sub>3</sub>N<sub>4</sub>@NH<sub>2</sub>-CB to be an alternative to Pt/C as an affordable metal-free ORR catalyst.

The electrocatalytic activity of as-synthesized 3-D porous P-g-C<sub>3</sub>N<sub>4</sub>@NH<sub>2</sub>-CB composite was further compared with various catalysts, including heteroatom-doped carbon materials (e.g., BCN-graphene, N-doped mesoporous carbon, N, S dual-doped graphene-CNT composite)<sup>23,24,42</sup> and carbon nitride based catalysts (e.g., g-C<sub>3</sub>N<sub>4</sub>@graphene composite, g-C<sub>3</sub>N<sub>4</sub>/rGO),<sup>27,31,32,43,44</sup> as shown in Table S1. Müllen et al. reported the N-doped mesoporous carbon with an onset potential of 0.83 V and a limiting current density of 4.30 mA cm<sup>-2</sup> at 0.4 V,<sup>24</sup> while Dai et al. synthesized the B-N dual-doped graphene materials exhibited a decent onset potential with a higher limiting current density of 4.45 mA cm<sup>-2</sup>.<sup>23</sup> The presence of the heteroatoms (e.g., N, B, S) was found to tune the spin and charge density of neighboring carbon, thereby improving the ORR activity of corresponding doped carbon materials.<sup>28</sup> However, the low heteroatom concentration combined with the

disordered structure of doped carbon materials still limits ORR performance of heteroatom-doped carbon materials. In sharp contrast, as-synthesized 3-D P-g-C<sub>3</sub>N<sub>4</sub>@NH<sub>2</sub>-CB composite contains a well-ordered tri-s-triazine ring structured P-g-C<sub>3</sub>N<sub>4</sub> NSs with high N concentration, and the synergistic effect between doped P atoms and pristine N atoms on neighboring carbon significantly improves the ORR activity of 3-D P-g-C<sub>3</sub>N<sub>4</sub>. In addition, the inserted NH<sub>2</sub>-CB effectively stabilizes the pre-exfoliated P-g-C<sub>3</sub>N<sub>4</sub> NSs and facilitates construction of a 3-D porous composite. Therefore, as-synthesized P-g-C<sub>3</sub>N<sub>4</sub>@NH<sub>2</sub>-CB exhibits a remarkable ORR performance that is much higher than those of reported heteroatom-doped carbon materials and carbon nitride base composites, such as g-C<sub>3</sub>N<sub>4</sub>@graphene composite, and g-C<sub>3</sub>N<sub>4</sub>/CNT.

In order to further investigate the ORR activity of P-g-C<sub>3</sub>N<sub>4</sub>@NH<sub>2</sub>-CB as well as the reaction mechanism, RRDE tests were conducted to directly measure the concentration of HO<sub>2</sub><sup>-</sup> intermediate and determine the electron transfer number (*n*) of ORR on these catalysts. The generated HO<sub>2</sub><sup>-</sup> intermediate on the surface of disk electrode can be immediately oxidized on the surface of a Pt ring electrode with a setting potential of 0.8 V vs RHE. As shown in Figure S11, P-g-C<sub>3</sub>N<sub>4</sub>@NH<sub>2</sub>-CB showed the lowest ring current density due to the HO<sub>2</sub><sup>-</sup> oxidation, and the HO<sub>2</sub><sup>-</sup> yield on disk electrode was constant at 12% between 0.25 to 0.55 V (Figure 4a), revealing that the disk current density mostly resulted from OH<sup>-</sup> production through 4e<sup>-</sup> transfer ORR reaction, and the average *n* value of P-g-C<sub>3</sub>N<sub>4</sub>@NH<sub>2</sub>-CB was determined to be 3.83 with little variations from 0.25 to 0.55 V (Figure 4a). On the other hand, the average HO<sub>2</sub><sup>-</sup> yield on P-g-C<sub>3</sub>N<sub>4</sub>@SO<sub>3</sub>H-CB and P-g-C<sub>3</sub>N<sub>4</sub> NSs were determined to be 26%, and 40% with the *n* value of 3.46 (P-g-C<sub>3</sub>N<sub>4</sub>@SO<sub>3</sub>H-CB), and 3.21 (P-g-C<sub>3</sub>N<sub>4</sub> NSs), respectively, which is in good agreement with the results derived from the K-L equation in RDE tests. The large amount of HO<sub>2</sub><sup>-</sup> intermediate production could decrease the *n* value and drastically reduce the ORR efficiency. Thus, the P-g-C<sub>3</sub>N<sub>4</sub>@NH<sub>2</sub>-CB with the lowest HO<sub>2</sub><sup>-</sup> yield exhibits the best ORR performance over three investigated P-g-C<sub>3</sub>N<sub>4</sub> materials. The positive-negative charge interaction between NH<sub>2</sub>-CB and P-g-C<sub>3</sub>N<sub>4</sub> sheets was expected to facilitate the NH<sub>2</sub>-CB insertion into P-g-C<sub>3</sub>N<sub>4</sub> NSs with the increasing of the layer distance, and more active sites were exposed, so as to greatly enhance the ORR performance of P-g-C<sub>3</sub>N<sub>4</sub> NSs. Furthermore, the good ORR activity on P-g-C<sub>3</sub>N<sub>4</sub>@NH<sub>2</sub>-CB is also suggested by the electrochemical impedance spectroscopy (EIS) results (Figure 4b). In the high frequency regime, the P-g-C<sub>3</sub>N<sub>4</sub> NSs and P-g-C<sub>3</sub>N<sub>4</sub>@NH<sub>2</sub>-CB exhibit a relatively smaller intercept in the real axis (*Z*<sub>Re</sub>) than that of g-C<sub>3</sub>N<sub>4</sub> NSs, revealing the lower contact resistance and ohmic resistance. The lower resistance of P-doped carbon nitride can be attributed to the incorporated P with lone pair electrons that can delocalize the  $\pi$ -conjugated tri-s-triazine of the same building unit, and facilitate the localization of the hole for charge transfer to increase the conductivity of P-g-C<sub>3</sub>N<sub>4</sub> materials.<sup>45</sup> On the other hand, the P-g-C<sub>3</sub>N<sub>4</sub>@NH<sub>2</sub>-CB shows the smallest semicircle in comparison with those on P-g-C<sub>3</sub>N<sub>4</sub> NSs and g-C<sub>3</sub>N<sub>4</sub> NSs (Figure 4b), indicating the fast kinetic process of ORR on P-g-C<sub>3</sub>N<sub>4</sub>@NH<sub>2</sub>-CB catalysts.<sup>36</sup> The high surface area with more exposed ORR active sites, owing to the 3-D porous configuration, endows P-g-C<sub>3</sub>N<sub>4</sub>@NH<sub>2</sub>-CB with higher ORR rate. Therefore, both the electrical and electrocatalytic properties of P-g-C<sub>3</sub>N<sub>4</sub>@NH<sub>2</sub>-CB were

promoted because of the insertion of NH<sub>2</sub>-CB driven by the positive-negative charge interaction with P-g-C<sub>3</sub>N<sub>4</sub> NSs.

The catalyst stability is another important criterion for evaluation of ORR catalysts. In this regard, P-g-C<sub>3</sub>N<sub>4</sub>@NH<sub>2</sub>-CB was further tested by cycling the catalyst at 10 mV s<sup>-1</sup> scan rate under oxygen purging. After 3000 potential cycles, the P-g-C<sub>3</sub>N<sub>4</sub>@NH<sub>2</sub>-CB exhibits a robust stability with only 47 mV of half-wave potential shift (Figure 5), which is superior to the 52

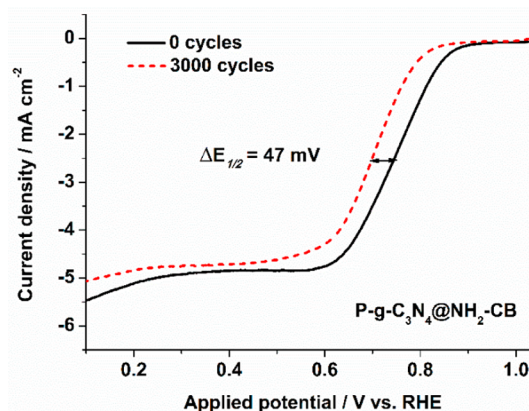


Figure 5. ORR polarization curves P-g-C<sub>3</sub>N<sub>4</sub>@NH<sub>2</sub>-CB before and after 3000 potential cycles in O<sub>2</sub>-saturated 0.1 M KOH solution.

mV observed on the commercial Pt/C catalyst (Figure S12). The stability of P-g-C<sub>3</sub>N<sub>4</sub>@NH<sub>2</sub>-CB was further measured at a constant voltage of 0.4 V for 36000 s (10 h). The results indicate a slow decrease of ORR activity of P-g-C<sub>3</sub>N<sub>4</sub>@NH<sub>2</sub>-CB, where 90.2% of the current was maintained after 36000 s (Figure S13). On the contrary, Pt/C shows more severe performance degradation, as only 75.6% of the current remained after an identical stability test (Figure S13). Together with the potential-cycle test results, the active and robust P-g-C<sub>3</sub>N<sub>4</sub>@NH<sub>2</sub>-CB composite electrocatalyst demonstrates its great potential to serve as a Pt/C alternative for ORR in fuel cells, Li-air batteries, and other energy storage and conversion devices with oxygen electrodes.

#### 4. CONCLUSIONS

In summary, we have demonstrated a successful synthesis of P-doped graphite-like carbon nitride nanosheets assembled with NH<sub>2</sub>-functionalized carbon black via an efficient exfoliation approach. The positively charged NH<sub>2</sub>-CB nanoparticles were self-assembled with negatively charged P-g-C<sub>3</sub>N<sub>4</sub>, which can significantly enhance the exfoliation performance to obtain thinner layered P-g-C<sub>3</sub>N<sub>4</sub> nanosheets with a thickness of <3 nm and high surface area of 286 m<sup>2</sup> g<sup>-1</sup>. The P atoms were then incorporated into the tri-s-triazine rings while 2-D layered structure was well maintained upon the P doping. The introduction of the NH<sub>2</sub>-CB facilitates its transformation to a 3-D composite material, which not only significantly enhances the ORR performance, but also greatly improves the electrical conductivity of P-g-C<sub>3</sub>N<sub>4</sub>@NH<sub>2</sub>-CB catalysts. As a result, the obtained P-g-C<sub>3</sub>N<sub>4</sub>@NH<sub>2</sub>-CB exhibits a remarkable ORR performance with an onset potential of 0.90 V vs RHE, Tafel slope of 89 mV dec<sup>-1</sup>, and electron transfer number of 3.83 per oxygen molecule in alkaline media. This is comparable to that recorded on Pt/Vulcan XC-72. Moreover, the better ORR stability with P-g-C<sub>3</sub>N<sub>4</sub>@NH<sub>2</sub>-CB as compared to Pt/Vulcan XC-72 suggests a promising alternative cathodic catalyst that

could substitute noble metals used in electrochemical energy conversion and storage devices.

## ■ ASSOCIATED CONTENT

### ● Supporting Information

The Supporting Information is available free of charge on the ACS Publications website at DOI: 10.1021/acs.langmuir.6b02498.

Additional details as described in the text (PDF)

## ■ AUTHOR INFORMATION

### Corresponding Author

\*E-mail: wzli@iastate.edu. Tel: +1-515-294-4582.

### Notes

The authors declare no competing financial interest.

## ■ ACKNOWLEDGMENTS

We acknowledge financial support from Iowa State University and Ames Lab Startup Funds, and Iowa Energy Center Opportunity Grant Fund. We are grateful to Dr. Dapeng Jing for XPS characterization on P-g-C<sub>3</sub>N<sub>4</sub> materials. W. Li thanks his Richard Seagrave Professorship support.

## ■ REFERENCES

- (1) Hoffert, M. I.; Caldeira, K.; Benford, G.; Criswell, D. R.; Green, C.; Herzog, H.; Jain, A. K.; Khesghi, H. S.; Lackner, K. S.; Lewis, J. S.; Lightfoot, H. D.; Manheimer, W.; Mankins, J. C.; Mauel, M. E.; Perkins, L. J.; Schlesinger, M. E.; Volk, T.; Wigley, T. M. L. Advanced technology paths to global climate stability: Energy for a greenhouse planet. *Science* **2002**, *298*, 981–987.
- (2) Huber, G. W.; Iborra, S.; Corma, A. Synthesis of transportation fuels from biomass: Chemistry, catalysts, and engineering. *Chem. Rev.* **2006**, *106*, 4044–4098.
- (3) Steele, B. C. H.; Heinzel, A. Materials for fuel-cell technologies. *Nature* **2001**, *414*, 345–352.
- (4) Weber, A. Z.; Mench, M. M.; Meyers, J. P.; Ross, P. N.; Gostick, J. T.; Liu, Q. H. Redox flow batteries: a review. *J. Appl. Electrochem.* **2011**, *41*, 1137–1164.
- (5) Cheng, F. Y.; Chen, J. Metal-air batteries: from oxygen reduction electrochemistry to cathode catalysts. *Chem. Soc. Rev.* **2012**, *41*, 2172–2192.
- (6) Dunn, B.; Kamath, H.; Tarascon, J. M. Electrical Energy Storage for the Grid: A Battery of Choices. *Science* **2011**, *334*, 928–935.
- (7) Xin, L.; Zhang, Z. Y.; Qi, J.; Chadderdon, D.; Li, W. Z. Electrocatalytic oxidation of ethylene glycol (EG) on supported Pt and Au catalysts in alkaline media: Reaction pathway investigation in three-electrode cell and fuel cell reactors. *Appl. Catal., B* **2012**, *125*, 85–94.
- (8) Zhang, Z. Y.; Xin, L.; Qi, J.; Chadderdon, D. J.; Li, W. Z. Supported Pt, Pd and Au nanoparticle anode catalysts for anion-exchange membrane fuel cells with glycerol and crude glycerol fuels. *Appl. Catal., B* **2013**, *136*, 29–39.
- (9) Gasteiger, H. A.; Kocha, S. S.; Sompalli, B.; Wagner, F. T. Activity benchmarks and requirements for Pt, Pt-alloy, and non-Pt oxygen reduction catalysts for PEMFCs. *Appl. Catal., B* **2005**, *56*, 9–35.
- (10) Merle, G.; Wessling, M.; Nijmeijer, K. Anion exchange membranes for alkaline fuel cells: A review. *J. Membr. Sci.* **2011**, *377*, 1–35.
- (11) Adzic, R. R.; Zhang, J.; Sasaki, K.; Vukmirovic, M. B.; Shao, M.; Wang, J. X.; Nilekar, A. U.; Mavrikakis, M.; Valerio, J. A.; Uribe, F. Platinum monolayer fuel cell electrocatalysts. *Top. Catal.* **2007**, *46*, 249–262.
- (12) Jaouen, F.; Proietti, E.; Lefevre, M.; Chenitz, R.; Dodelet, J. P.; Wu, G.; Chung, H. T.; Johnston, C. M.; Zelenay, P. Recent advances in non-precious metal catalysis for oxygen-reduction reaction in polymer electrolyte fuel cells. *Energy Environ. Sci.* **2011**, *4*, 114–130.
- (13) Gorlin, Y.; Chung, C. J.; Nordlund, D.; Clemens, B. M.; Jaramillo, T. F. Mn<sub>3</sub>O<sub>4</sub> Supported on Glassy Carbon: An Active Non-Precious Metal Catalyst for the Oxygen Reduction Reaction. *ACS Catal.* **2012**, *2*, 2687–2694.
- (14) Liang, Y.; Li, Y.; Wang, H.; Zhou, J.; Wang, J.; Regier, T.; Dai, H. Co<sub>3</sub>O<sub>4</sub> nanocrystals on graphene as a synergistic catalyst for oxygen reduction reaction. *Nat. Mater.* **2011**, *10*, 780–786.
- (15) Zhang, Z. Z.; More, K. L.; Sun, K.; Wu, Z. L.; Li, W. Z. Preparation and Characterization of PdFe Nanoleaves as Electrocatalysts for Oxygen Reduction Reaction. *Chem. Mater.* **2011**, *23*, 1570–1577.
- (16) Gong, K. P.; Du, F.; Xia, Z. H.; Durstock, M.; Dai, L. M. Nitrogen-Doped Carbon Nanotube Arrays with High Electrocatalytic Activity for Oxygen Reduction. *Science* **2009**, *323*, 760–764.
- (17) Yang, Z.; Yao, Z.; Li, G. F.; Fang, G. Y.; Nie, H. G.; Liu, Z.; Zhou, X. M.; Chen, X.; Huang, S. M. Sulfur-Doped Graphene as an Efficient Metal-free Cathode Catalyst for Oxygen Reduction. *ACS Nano* **2012**, *6*, 205–211.
- (18) Liang, J.; Jiao, Y.; Jaroniec, M.; Qiao, S. Z. Sulfur and Nitrogen Dual-Doped Mesoporous Graphene Electrocatalyst for Oxygen Reduction with Synergistically Enhanced Performance. *Angew. Chem., Int. Ed.* **2012**, *51*, 11496–11500.
- (19) Zhang, L. P.; Xia, Z. H. Mechanisms of Oxygen Reduction Reaction on Nitrogen-Doped Graphene for Fuel Cells. *J. Phys. Chem. C* **2011**, *115*, 11170–11176.
- (20) Dai, L. M.; Xue, Y. H.; Qu, L. T.; Choi, H. J.; Baek, J. B. Metal-Free Catalysts for Oxygen Reduction Reaction. *Chem. Rev.* **2015**, *115*, 4823–4892.
- (21) Wang, D. W.; Su, D. S. Heterogeneous nanocarbon materials for oxygen reduction reaction. *Energy Environ. Sci.* **2014**, *7*, 576–591.
- (22) Qiu, Y.; Huo, J. J.; Jia, F.; Shanks, B. H.; Li, W. Z. N- and S-doped mesoporous carbon as metal-free cathode catalysts for direct biorenewable alcohol fuel cells. *J. Mater. Chem. A* **2016**, *4*, 83–95.
- (23) Wang, S. Y.; Zhang, L. P.; Xia, Z. H.; Roy, A.; Chang, D. W.; Baek, J. B.; Dai, L. M. BCN Graphene as Efficient Metal-Free Electrocatalyst for the Oxygen Reduction Reaction. *Angew. Chem., Int. Ed.* **2012**, *51*, 4209–4212.
- (24) Liu, R. L.; Wu, D. Q.; Feng, X. L.; Müllen, K. Nitrogen-Doped Ordered Mesoporous Graphitic Arrays with High Electrocatalytic Activity for Oxygen Reduction. *Angew. Chem., Int. Ed.* **2010**, *49*, 2565–2569.
- (25) Niu, P.; Zhang, L. L.; Liu, G.; Cheng, H. M. Graphene-Like Carbon Nitride Nanosheets for Improved Photocatalytic Activities. *Adv. Funct. Mater.* **2012**, *22*, 4763–4770.
- (26) Yang, S. B.; Gong, Y. J.; Zhang, J. S.; Zhan, L.; Ma, L. L.; Fang, Z. Y.; Vajtai, R.; Wang, X. C.; Ajayan, P. M. Exfoliated Graphitic Carbon Nitride Nanosheets as Efficient Catalysts for Hydrogen Evolution Under Visible Light. *Adv. Mater.* **2013**, *25*, 2452–2456.
- (27) Fu, X. R.; Hu, X. F.; Yan, Z. H.; Lei, K. X.; Li, F. J.; Cheng, F. Y.; Chen, J. Template-free synthesis of porous graphitic carbon nitride/carbon composite spheres for electrocatalytic oxygen reduction reaction. *Chem. Commun.* **2016**, *52*, 1725–1728.
- (28) Ma, T. Y.; Dai, S.; Jaroniec, M.; Qiao, S. Z. Graphitic Carbon Nitride Nanosheet-Carbon Nanotube Three-Dimensional Porous Composites as High-Performance Oxygen Evolution Electrocatalysts. *Angew. Chem., Int. Ed.* **2014**, *53*, 7281–7285.
- (29) Zheng, Y.; Jiao, Y.; Chen, J.; Liu, J.; Liang, J.; Du, A.; Zhang, W. M.; Zhu, Z. H.; Smith, S. C.; Jaroniec, M.; Lu, G. Q.; Qiao, S. Z. Nanoporous Graphitic-C<sub>3</sub>N<sub>4</sub>@Carbon Metal-Free Electrocatalysts for Highly Efficient Oxygen Reduction. *J. Am. Chem. Soc.* **2011**, *133*, 20116–20119.
- (30) Zhang, X. D.; Wang, H. X.; Wang, H.; Zhang, Q.; Xie, J. F.; Tian, Y. P.; Wang, J.; Xie, Y. Single-Layered Graphitic-C<sub>3</sub>N<sub>4</sub> Quantum Dots for Two-Photon Fluorescence Imaging of Cellular Nucleus. *Adv. Mater.* **2014**, *26*, 4438–4443.
- (31) Yang, S. B.; Feng, X. L.; Wang, X. C.; Müllen, K. Graphene-Based Carbon Nitride Nanosheets as Efficient Metal-Free Electrocatalysts for Oxygen Reduction Reactions. *Angew. Chem., Int. Ed.* **2011**, *50*, 5339–5343.

(32) Liang, J.; Zheng, Y.; Chen, J.; Liu, J.; Hulicova-Jurcakova, D.; Jaroniec, M.; Qiao, S. Z. Facile Oxygen Reduction on a Three-Dimensionally Ordered Macroporous Graphitic C<sub>3</sub>N<sub>4</sub>/Carbon Composite Electrocatalyst. *Angew. Chem., Int. Ed.* **2012**, *51*, 3892–3896.

(33) Xin, L.; Yang, F.; Rasouli, S.; Qiu, Y.; Li, Z. F.; Uzunoglu, A.; Sun, C. J.; Liu, Y. Z.; Ferreira, P.; Li, W. Z.; Ren, Y.; Stanciu, L. A.; Xie, J. Understanding Pt nanoparticle anchoring on graphene supports through surface functionalization. *ACS Catal.* **2016**, *6*, 2642–2653.

(34) Li, Z. F.; Xin, L.; Yang, F.; Liu, Y. D.; Liu, Y. Z.; Zhang, H. Y.; Stanciu, L.; Xie, J. Hierarchical polybenzimidazole-grafted graphene hybrids as supports for Pt nanoparticle catalysts with excellent PEMFC performance. *Nano Energy* **2015**, *16*, 281–292.

(35) Qiu, Y.; Xin, L.; Li, W. Z. Electrocatalytic Oxygen Evolution over Supported Small Amorphous Ni-Fe Nanoparticles in Alkaline Electrolyte. *Langmuir* **2014**, *30*, 7893–7901.

(36) Wang, Z. C.; Xin, L.; Zhao, X. S.; Qiu, Y.; Zhang, Z. Y.; Baturina, O. A.; Li, W. Z. Carbon supported Ag nanoparticles with different particle size as cathode catalysts for anion exchange membrane direct glycerol fuel cells. *Renewable Energy* **2014**, *62*, 556–562.

(37) Zhang, X. D.; Xie, X.; Wang, H.; Zhang, J. J.; Pan, B. C.; Xie, Y. Enhanced Photoresponsive Ultrathin Graphitic-Phase C<sub>3</sub>N<sub>4</sub> Nanosheets for Bioimaging. *J. Am. Chem. Soc.* **2013**, *135*, 18–21.

(38) Zhu, Y. P.; Ren, T. Z.; Yuan, Z. Y. Mesoporous Phosphorus-Doped g-C<sub>3</sub>N<sub>4</sub> Nanostructured Flowers with Superior Photocatalytic Hydrogen Evolution Performance. *ACS Appl. Mater. Interfaces* **2015**, *7*, 16850–16856.

(39) Zhou, Y. J.; Zhang, L. X.; Liu, J. J.; Fan, X. Q.; Wang, B. Z.; Wang, M.; Ren, W. C.; Wang, J.; Li, M. L.; Shi, J. L. Brand new P-doped g-C<sub>3</sub>N<sub>4</sub>: enhanced photocatalytic activity for H<sub>2</sub> evolution and Rhodamine B degradation under visible light. *J. Mater. Chem. A* **2015**, *3*, 3862–3867.

(40) Zhang, J. T.; Zhao, Z. H.; Xia, Z. H.; Dai, L. M. A metal-free bifunctional electrocatalyst for oxygen reduction and oxygen evolution reactions. *Nat. Nanotechnol.* **2015**, *10*, 444–452.

(41) Ma, T. Y.; Ran, J. R.; Dai, S.; Jaroniec, M.; Qiao, S. Z. Phosphorus-Doped Graphitic Carbon Nitrides Grown In Situ on Carbon-Fiber Paper: Flexible and Reversible Oxygen Electrodes. *Angew. Chem., Int. Ed.* **2015**, *54*, 4646–4650.

(42) Higgins, D. C.; Hoque, M. A.; Hassan, F.; Choi, J. Y.; Kim, B.; Chen, Z. W. Oxygen Reduction on Graphene-Carbon Nanotube Composites Doped Sequentially with Nitrogen and Sulfur. *ACS Catal.* **2014**, *4*, 2734–2740.

(43) Tian, J. Q.; Ning, R.; Liu, Q.; Asiri, A. M.; Al-Youbi, A. O.; Sun, X. P. Three-Dimensional Porous Supramolecular Architecture from Ultrathin g-C<sub>3</sub>N<sub>4</sub> Nanosheets and Reduced Graphene Oxide: Solution Self-Assembly Construction and Application as a Highly Efficient Metal-Free Electrocatalyst for Oxygen Reduction Reaction. *ACS Appl. Mater. Interfaces* **2014**, *6*, 1011–1017.

(44) Qiu, K. P.; Guo, Z. X. Hierarchically porous graphene sheets and graphitic carbon nitride intercalated composites for enhanced oxygen reduction reaction. *J. Mater. Chem. A* **2014**, *2*, 3209–3215.

(45) Zhang, Y. J.; Mori, T.; Ye, J. H.; Antonietti, M. Phosphorus-Doped Carbon Nitride Solid: Enhanced Electrical Conductivity and Photocurrent Generation. *J. Am. Chem. Soc.* **2010**, *132*, 6294–6295.